

Preparation and visible-light photocatalytic performances of g-C₃N₄ surface hybridized with a small amount of CdS nanoparticles

Desong Wang¹ · Zexuan Xu¹ · Qingzhi Luo¹ · Xueyan Li¹ · Jing An¹ · Rong Yin¹ · Cai Bao²

Received: 6 July 2015 / Accepted: 4 September 2015 / Published online: 18 September 2015
© Springer Science+Business Media New York 2015

Abstract An efficient visible-light photocatalyst was successfully synthesized by surface-hybridizing graphitic carbon nitride (g-C₃N₄) using a small amount of cadmium sulfide (CdS) nanoparticles. The CdS/g-C₃N₄ nanocomposites were characterized by X-ray diffraction, X-ray photoelectron spectroscopy, Raman spectroscopy, scanning electron microscopy, transmission electron microscopy, UV–Vis diffuse reflectance spectroscopy, photoluminescence spectroscopy, electrochemical impedance spectroscopy, and photocurrent–time measurement. The photocatalytic activity of the CdS/g-C₃N₄ nanocomposites was investigated by evaluating the degradation of Rhodamine B (RhB) under visible-light irradiation. The effects of the CdS content on the nanocomposites, initial RhB concentration, pH value of the investigated system, and dosage of CdS/g-C₃N₄ nanocomposites on the visible-light photocatalytic activity were systematically investigated. The results revealed that the visible-light photocatalytic activity of g-C₃N₄-based photocatalysts was significantly improved by surface-hybridization of a small amount of CdS nanoparticles, increased as both CdS content on the nanocomposites and dosage of CdS/g-C₃N₄ nanocomposites increased, while increased at first and then decreased as

both initial RhB concentration and pH value of the investigated system increased. The visible-light photocatalytic mechanism of the CdS/g-C₃N₄ nanocomposites was discussed.

Introduction

The semiconductor photocatalysts have attracted much attention in several application fields including degradation of organic pollutants in water and production of hydrogen and/or oxygen via water splitting under light irradiation [1–5]. Among these semiconductor photocatalysts, TiO₂ has been regarded as one of the most promising photocatalysts due to its high chemical stability, superior reusability, low cost, and low toxicity [6–8]. However, the wide band gap of anatase TiO₂ (3.2 eV) leads it to low efficiency in utilization of visible light. Therefore, several approaches, such as metal or nonmetal doping [9, 10], noble metal deposition, and conjugated polymer modification [11, 12], have been developed to improve the visible-light photocatalytic activity of the TiO₂ photocatalyst. Meanwhile, some new visible-light photocatalysts, such as silver halide [13], silver phosphate [14], sulfides [15], vanadates [16], BiXO (X = Br, I) [17], and graphitic-like carbon nitride (g-C₃N₄) [18], have been prepared and investigated in detail.

Recently, the g-C₃N₄ photocatalyst has drawn a lot of interests in visible-light photocatalytic applications owing to its easy production and superior chemical stability [19, 20]. Nevertheless, the high recombination probability of photogenerated electron–hole pairs leads g-C₃N₄ to exhibiting low photocatalytic activity under visible-light irradiation, and g-C₃N₄ can be only excited by the visible light with the wavelength <450 nm due to its medium-

Electronic supplementary material The online version of this article (doi:10.1007/s10853-015-9417-y) contains supplementary material, which is available to authorized users.

✉ Desong Wang
dswang06@126.com; wangdesong@hebust.edu.cn

¹ School of Sciences, Hebei University of Science and Technology, Shijiazhuang 050018, China

² College of Chemical and Pharmaceutical Engineering, Hebei University of Science and Technology, Shijiazhuang 050018, Hebei, China

band gap of ca. 2.7 eV, indicating that g-C₃N₄ cannot efficiently utilize the visible light with longer wavelength (>450 nm) to degrade organic pollutants and to produce hydrogen and oxygen via water splitting [21–25]. Therefore, many strategies have been developed to overcome the above-mentioned drawbacks, such as doping with metal or nonmetal elements, coupling with other semiconductors (e.g., WO₃, CdS, AgX, graphene, reduced graphene oxide, TiO₂, ZnO) [26–30], and modifying by conjugated polymers [30, 31].

Among these strategies, coupling g-C₃N₄ with CdS, a semiconductor with narrow band gap of 2.5 eV [32], has become a promising technique to prepare an efficient visible-light photocatalyst because of higher separation efficiency of photogenerated hole/electron pairs in CdS/g-C₃N₄ composite and efficient utilization of visible light with longer wavelength of 450 nm. Ge et al. [33] prepared CdS/g-C₃N₄ composite photocatalysts by coupling g-C₃N₄ powders with CdS quantum dots, Zhang et al. [34] prepared CdS/g-C₃N₄ core/shell nanowires using a combined solvothermal and chemisorption method, and Cao et al. [35] synthesized g-C₃N₄ nanosheets modified by CdS quantum dots through a solvothermal method. The CdS-modified g-C₃N₄ powders, nanowires, and nanosheets exhibited obviously improved hydrogen evolution rate via water splitting under visible-light irradiation. Fu et al. [36] prepared CdS/g-C₃N₄ composite photocatalysts via an “in situ” precipitation–deposition method, and Jiang et al. [37] fabricated CdS/g-C₃N₄ composite photocatalyst via a precipitation method. They found that the composite photocatalysts degraded organic compounds more efficiently than pure g-C₃N₄ under visible light. Dai et al. [38] investigated selective oxidation of aromatic alcohols to aromatic aldehydes and reduction of nitrobenzene into aniline using CdS/g-C₃N₄ composite as a photocatalyst under visible-light illumination. However, the above-mentioned investigations mainly dealt with CdS/g-C₃N₄ composites containing CdS more than 10 %, a larger amount of CdS in the composites can possibly cause a new environmental pollution due to the significant hazardousness of Cd²⁺. Therefore, it is a meaningful investigation to prepare an efficient CdS/g-C₃N₄ photocatalyst containing a small amount of CdS (≤1 %). So far, to the best of our knowledge, little work was investigated on the composite photocatalyst with the CdS content of <1 %.

In this work, the CdS/g-C₃N₄ composite photocatalysts were prepared via a surface-hybridization of g-C₃N₄ using a small amount of CdS nanoparticles. The as-prepared nanocomposites were characterized by X-ray diffraction (XRD), X-ray photoelectron spectroscopy (XPS), Raman spectroscopy, scanning electron microscopy (SEM), transmission electron microscopy (TEM), UV–Vis diffuse reflectance spectroscopy (DRS), photoluminescence

spectroscopy (PL), electrochemical impedance spectroscopy (EIS), and photocurrent–time measurement (PT). The photocatalytic activity and stability were investigated by evaluating the photodegradation of Rhodamine B (RhB) under visible-light irradiation, and the main affecting factors of the visible-light photocatalytic activity were discussed.

Experimental

Reagents and materials

Cadmium acetate was purchased from Tianjin Guangfu Fine Chemical Research Institute. Sodium sulfide was obtained from Tianjin Bodi Chemical Company. Melamine and phenol were purchased from Aladdin Company. All the above reagents were of AR grade and used without further purification. All the solutions were prepared using deionized water.

Preparation of photocatalysts

The g-C₃N₄ samples were prepared by directly heating melamine in a semi-closed system according to the literature [39, 40]. In a typical preparation process, 20 g of melamine was firstly heated in a muffle furnace from room temperature to 520 °C with a heating rate of 2 °C min⁻¹. After heating at 520 °C for 2 h, the as-prepared g-C₃N₄ was cooled naturally to room temperature, and then was grinded for further use.

The CdS/g-C₃N₄ composite photocatalysts were prepared according to the following steps. Firstly, a designed amount of cadmium acetate was dissolved in 50 g of deionized water. Secondly, 2.0 g of g-C₃N₄ powders was added into the cadmium acetate solution under ultrasonic conditions. After ultrasonification for 10 min, the obtained suspension was heated at 100 °C to obtain a dried mixture of g-C₃N₄ and cadmium acetate via solvent volatilization. Thirdly, the dried mixture was added into a sodium sulfide solution to form a CdS/g-C₃N₄ nanocomposite through a precipitation method. The as-prepared CdS/g-C₃N₄ nanocomposites with different CdS contents were labeled as CdS/g-C₃N₄(*x* %), where *x* % is the content of CdS in the CdS/g-C₃N₄ nanocomposites.

Characterization of photocatalysts

The XRD patterns of the CdS/g-C₃N₄ nanocomposites and pure g-C₃N₄ were measured in the range of $2\theta = 10^\circ\text{--}80^\circ$ by continuous scanning on a Rigaku, D/MAX-2500 diffractometer (Rigaku Co., Japan) with Cu *K*_α radiation ($\lambda = 0.15406$ nm). The operated voltage and current were 40 kV and 100 mA, respectively. XPS measurements were

performed using a PHI 5000C ESCA system with Al $K\alpha$ radiation ($h\nu = 1486.6$ eV) at a detection angle of 54° . The X-ray anode was run at 250 W, and the high voltage was kept at 15.0 kV. Raman spectroscopy was performed by a Nicolet 6700 Raman microspectrometer at a resolution of 2 cm^{-1} , an Ar ion laser with the line of 514.5 nm was used as the excitation source, and the accelerating voltage and emission current were 30 kV and 30 mA, respectively. The emission SEM was performed using a HITACHI S-4800-I emission scanning electron microscope operated at accelerating voltage of 10 kV. The TEM measurement was performed using a JEM 2100 transmission electron microscope, and the operating voltage was 200 kV. UV–Vis DRS was performed on a SHIMADZU-2550 Scan UV–Vis system equipped with an integrating sphere attachment (Shimadzu Co., Japan) in the range of 200–800 nm, and BaSO_4 was used as the background. The photoluminescence emission spectra (PL) of samples were detected by a Fluorescence spectrophotometer (F-4600 FL Spectrophotometer, Hitachi, Japan) at room temperature. The excitation source and light wavelength were a Xenon lamp and 316 nm, respectively. Electrochemical impedance spectra (EIS) were measured by an electrochemical system (Solartron 1255B frequency response analyzer and Solartron SI 1287 electrochemical interface) which was using 0.1 M KCl solution as the electrolyte, platinum electrode as counter electrode, saturated calomel electrode (SCE) as reference electrode, and FTO/CdS/g- C_3N_4 or FTO/g- C_3N_4 electrode as the working electrode. CdS/g- C_3N_4 and g- C_3N_4 films were coated by a doctor-blade method on the FTO substrates (fluorine-doped SnO_2 , $15\Omega/\text{sq}$). PT was measured on an electrochemical workstation (CHI660E, CHI Shanghai, Inc.), and 0.5 M Na_2SO_4 solution was used as the electrolyte, platinum electrode as counter electrode, Ag/AgCl electrode as reference electrode, and CdS/g- C_3N_4 or g- C_3N_4 electrode as the working electrode. The Brunauer–Emmett–Teller (BET) surface area measurements were performed using a Micromeritics TriStar II 3020 surface area and porosity system using nitrogen as adsorption gas at 77 K.

Photocatalytic activity measurement

The visible-light photocatalytic activity of the investigated materials was evaluated by RhB and phenol photodegradation. The photocatalytic degradation of RhB or phenol was carried out by decomposing RhB solutions (100 mL , 4 mg L^{-1}) or phenol solution (100 mL , 20 mg L^{-1}) containing 0.10 g of photocatalysts under visible-light irradiation. Before irradiation, the suspensions were continuously stirred for 1 h in the dark to establish adsorption/desorption equilibrium of RhB (or phenol) between the RhB (or phenol) solution and the photocatalyst

surface. Afterward, a 300 W iodine tungsten lamp (Philips Co.) was used as a visible-light source with a 400 nm optical filter, and the luminous intensity on the liquid surface was ca. 85.0 mW cm^{-2} measured by an optical power meter (Model 842-PE, Newport Corporation, USA). During the irradiation period, the samples were taken out every 30 min or 1 h from the reactor, and then the photocatalysts were separated from the suspension by high-speed centrifugation. The clarified solution was analyzed by a T6 UV–Vis spectrometer (Beijing Purkinje General Instruments Co., Ltd., China), and the absorbance of RhB and phenol was measured at their maximum absorption wavelengths of 554 and 270 nm, respectively. The symbols of c_0 and c are the concentrations of the RhB or phenol solution before and after photoirradiation, respectively.

Results and discussion

Characterization of CdS/g- C_3N_4 nanocomposites

Figure 1a illustrates the XRD patterns of pure CdS, pure g- C_3N_4 , and CdS/g- C_3N_4 nanocomposite photocatalysts. The two distinct diffraction peaks at 27.7° and 13.1° in the XRD spectrum of pure g- C_3N_4 can be indexed as the (002) and (100) planes, which come from the interlayer stacking of aromatic segments and in-plane structural packing motif, respectively. The three characteristic peaks at 52.06° , 43.98° , and 26.41° in the XRD pattern of pure CdS can be described to the (311), (220), and (111) planes of cubic CdS (JCPDS No.10-0454). From the XRD spectra of CdS/g- C_3N_4 nanocomposite photocatalysts, the two characteristic peaks of g- C_3N_4 are clearly observed, while the characteristic peaks of CdS are not observed because of its low content in the nanocomposites. The magnified XRD spectra of the nanocomposites (Fig. 1b) display a peak at 43.98° , which is ascribed to the characteristic one of cubic CdS. This result confirms the existence of CdS in the CdS/g- C_3N_4 nanocomposite photocatalysts.

XPS analysis is widely used to determine the chemical composition of the materials surface. The XPS survey spectra of the investigated samples are displayed in Fig. 2. The signals of C, N, O, Cd, and S can be observed from XPS spectrum of CdS/g- C_3N_4 (1 %), while only the signals of C, N, and O can be observed from that of pure g- C_3N_4 . The element of N originates from g- C_3N_4 , the element of C is attributed to g- C_3N_4 and adventitious elemental carbon, both Cd and S are ascribed to CdS, and O comes from the environment. This result and EDS result shown in Fig. S1 further confirm that the CdS exactly exists on the g- C_3N_4 surface, accordant with the XRD result.

Figure 3 shows the Raman spectra of CdS/g- C_3N_4 (1 %), pure g- C_3N_4 , and pure CdS. No characteristic peaks of pure

Fig. 1 XRD patterns of pure CdS, pure $g\text{-C}_3\text{N}_4$, and CdS/ $g\text{-C}_3\text{N}_4$ nanocomposites (a), and magnified XRD patterns of CdS/ $g\text{-C}_3\text{N}_4$ nanocomposites (b)

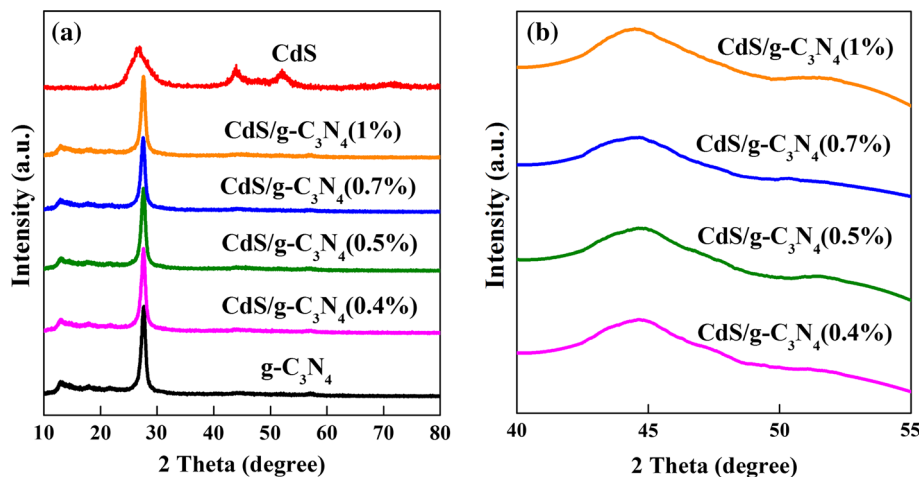


Fig. 2 XPS survey spectra of pure $g\text{-C}_3\text{N}_4$ (a) and CdS/ $g\text{-C}_3\text{N}_4$ (1 %) (b)

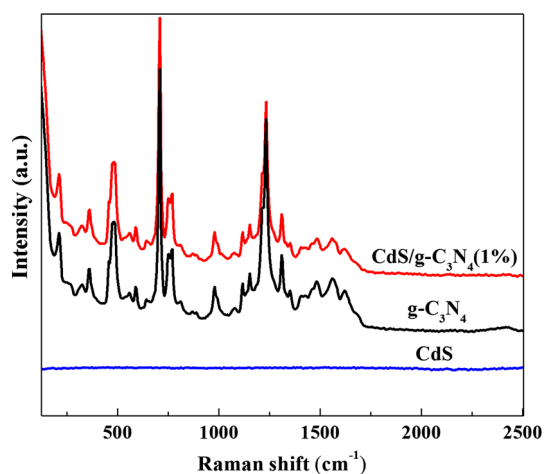
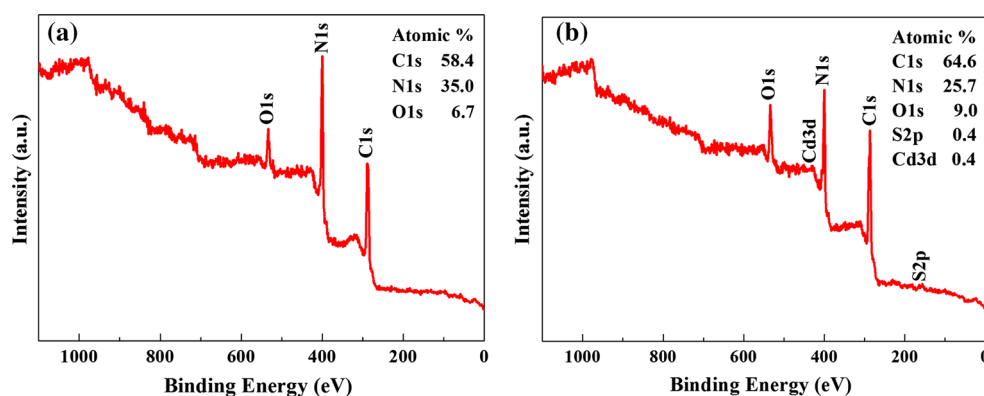


Fig. 3 Raman spectra of CdS/ $g\text{-C}_3\text{N}_4$ (1 %), pure $g\text{-C}_3\text{N}_4$, and pure CdS

CdS can be observed in its Raman spectrum, and the Raman spectrum of CdS/ $g\text{-C}_3\text{N}_4$ (1 %) is same as that of pure $g\text{-C}_3\text{N}_4$, indicating that the existence of CdS does not change the chemical composition of $g\text{-C}_3\text{N}_4$.

The morphology and microstructure of CdS/ $g\text{-C}_3\text{N}_4$ (1 %) and pure $g\text{-C}_3\text{N}_4$ were investigated by SEM and TEM, and the results are shown in Figs. 4 and 5, respectively. The SEM images in Fig. 4 show that both CdS/ $g\text{-C}_3\text{N}_4$ (1 %) and pure $g\text{-C}_3\text{N}_4$ display layered structure, and the morphology of the two samples is similar to each other except for the broken evidence of CdS/ $g\text{-C}_3\text{N}_4$ (1 %) due to its ultrasonication treatment. The TEM images in Fig. 5 further reveal the layered structure of pure $g\text{-C}_3\text{N}_4$ and CdS/ $g\text{-C}_3\text{N}_4$ (1 %). The CdS nanoparticles with the size of about 5 nm obviously aggregate and contact with $g\text{-C}_3\text{N}_4$ (Fig. 5b). The HRTEM image (set in Fig. 5b) of CdS nanoparticles exhibits fringe spacing of 0.337, 0.206, and 0.176 nm, which are ascribed to the (111), (220), and (311) lattice planes of cubic CdS (JSPDS-10-0454), respectively.

The UV–Vis diffuse reflectance spectra (DRS) of pure $g\text{-C}_3\text{N}_4$ and CdS/ $g\text{-C}_3\text{N}_4$ nanocomposites are shown in Fig. 6. As can be seen clearly, the absorption of the CdS/ $g\text{-C}_3\text{N}_4$ nanocomposites is obviously higher than that of pure $g\text{-C}_3\text{N}_4$ in the range of 200–550 nm, and increases with the CdS content increasing. The improved absorption in the range of 450–550 nm is advantageous to photocatalytic

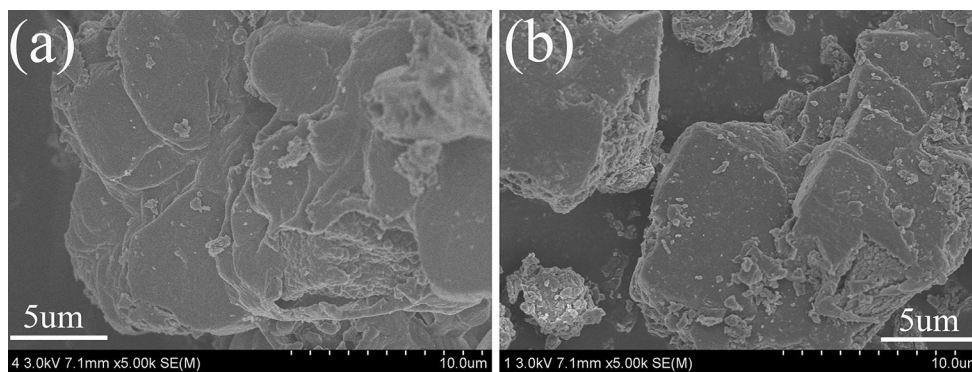


Fig. 4 SEM images of pure g-C₃N₄ (a) and CdS/g-C₃N₄(1 %) (b)

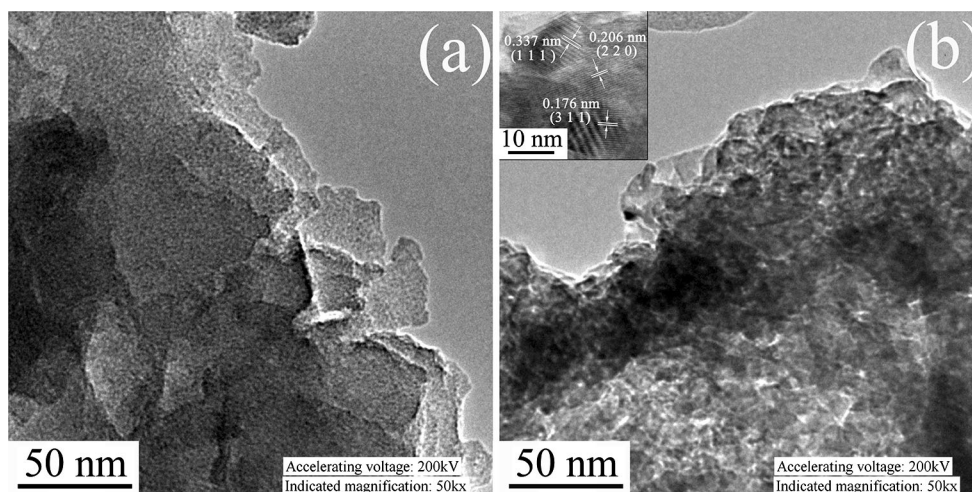


Fig. 5 TEM images of pure g-C₃N₄ (a) and CdS/g-C₃N₄(1 %) (b)

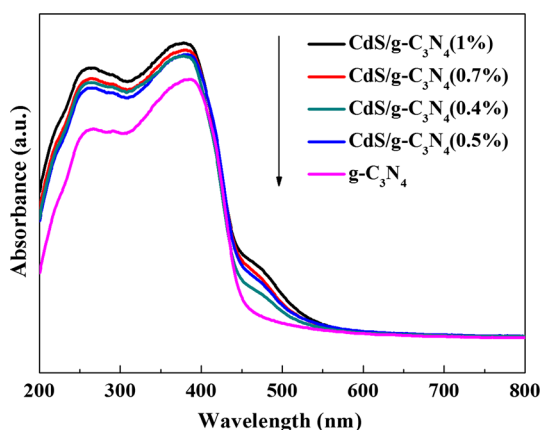


Fig. 6 UV-Vis diffuse reflectance spectra of pure g-C₃N₄ and CdS/g-C₃N₄ nanocomposites

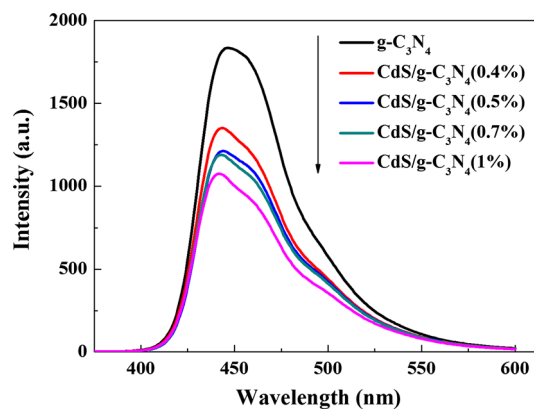


Fig. 7 PL spectra of pure g-C₃N₄ and the CdS/g-C₃N₄ nanocomposites

activity of CdS/g-C₃N₄ nanocomposites under visible-light irradiation.

Figure 7 displays the PL spectra of pure g-C₃N₄ and the CdS/g-C₃N₄ nanocomposites. A characteristic peak of PL

spectra can be easily observed at about 450 nm, which is ascribed to the recombination of photogenerated electrons and holes in semiconductors [41]. The peak intensity of CdS/g-C₃N₄ nanocomposites is significantly lower than

that of pure $g\text{-C}_3\text{N}_4$, and further weakens as the CdS content increases. This result indicates that the separation efficiency of photogenerated electron–hole pairs in CdS/ $g\text{-C}_3\text{N}_4$ nanocomposites is enhanced, and the larger content of CdS in the nanocomposites favors the improvement in separation efficiency of photogenerated electron–hole pairs.

The EIS is a useful tool to investigate the charge transfer rate at semiconductor/electrolyte interface in the dark [42]. The EIS Nyquist plots of FTO/ $g\text{-C}_3\text{N}_4$ electrode and FTO/CdS/ $g\text{-C}_3\text{N}_4$ (1 %) electrode are shown in Fig. 8. Compared with FTO/ $g\text{-C}_3\text{N}_4$ electrode, FTO/CdS/ $g\text{-C}_3\text{N}_4$ (1 %) electrode exhibits a smaller arc radius on its EIS Nyquist plot, revealing that the separation efficiency of charges in CdS/ $g\text{-C}_3\text{N}_4$ (1 %) can be increased. This result can be further confirmed by the photocurrent (I_{ph}) measurement which displays greatly enhanced photocurrents of the nanocomposites over pure $g\text{-C}_3\text{N}_4$ (Fig. S2). The improved separation efficiency of charges in the nanocomposites is advantageous to their visible-light photocatalytic activity.

Visible-light photocatalytic activity of CdS/ $g\text{-C}_3\text{N}_4$ nanocomposites

Figure 9a shows the RhB photodegradation under visible-light irradiation in the presence of pure $g\text{-C}_3\text{N}_4$ and CdS/ $g\text{-C}_3\text{N}_4$ nanocomposites. The photodegradation rate of RhB in the presence of the nanocomposites is obviously higher than that of pure $g\text{-C}_3\text{N}_4$, indicating that the nanocomposites exhibit enhanced visible-light photocatalytic activity. The relationship between $\ln(c_0/c)$ and irradiation time, shown in Fig. 9b, reveals that the kinetics of RhB photodecomposition on the surface of investigated photocatalysts can be described by the apparent first-order reaction [43]. The photodegradation rate constants k of RhB can be obtained from the slopes of the straight lines in Fig. 9b. The values of k reveal that the visible-light

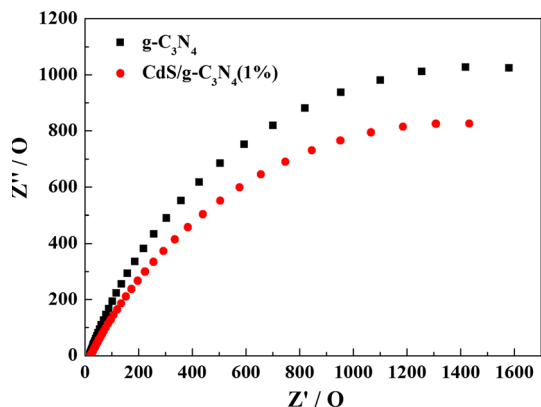


Fig. 8 EIS of FTO/ $g\text{-C}_3\text{N}_4$ and FTO/CdS/ $g\text{-C}_3\text{N}_4$ (1 %) electrodes with an applied bias potential of -0.5 V

photocatalytic activity of CdS/ $g\text{-C}_3\text{N}_4$ (0.3 %) is 1.9 times of that of pure $g\text{-C}_3\text{N}_4$, indicating that a small amount of CdS nanoparticles can greatly improve the visible-light photocatalytic activity of $g\text{-C}_3\text{N}_4$ photocatalyst.

For eliminating the sensitization effect of RhB, phenol, a colorless and widely used in photocatalysis investigations, was chosen as a second model pollutant. The results of phenol photodegradation catalyzed by pure $g\text{-C}_3\text{N}_4$ and CdS/ $g\text{-C}_3\text{N}_4$ (1 %) under visible-light irradiation are presented in Fig. 10. As can be clearly seen from Fig. 10, the phenol photodegradation rate content (0.0724 h^{-1}) in the presence of CdS/ $g\text{-C}_3\text{N}_4$ (1 %) is obviously higher than that (0.0386 h^{-1}) of pure $g\text{-C}_3\text{N}_4$, further confirming that the nanocomposite exhibits enhanced visible-light photocatalytic activity.

To further confirm RhB degradation photocatalyzed by CdS/ $g\text{-C}_3\text{N}_4$ (1 %) under visible-light irradiation, we have carried out the total organic carbon (TOC) measurement (TOC-VCPH, Shimadzu, Japan), and the result is shown in Fig. S3. The RhB solution (10 mg L^{-1}) was nearly decolorized after 3 h under visible-light irradiation, and about 90 % decrease of TOC is observed after 12 h, indicating that RhB has been not only decolorized but also mineralized efficiently.

Besides the photocatalytic activity, the photocatalytic stability is another essential factor for a photocatalyst [44]. The photocatalytic stability of CdS/ $g\text{-C}_3\text{N}_4$ (1 %) was investigated by the recycling experiments. After every cycle, the suspension was filtered to regenerate the photocatalysts and reused in the next cycle. Figure 11 shows that the photodegradation degree of RhB decreases a little with the recycling runs increasing, indicating that CdS/ $g\text{-C}_3\text{N}_4$ (1 %) exhibits good visible-light photocatalytic stability.

Affecting factors of RhB photodegradation

CdS content in CdS/ $g\text{-C}_3\text{N}_4$ nanocomposites

Figure 9 displays the effect of CdS content in CdS/ $g\text{-C}_3\text{N}_4$ nanocomposites on their visible-light photocatalytic activity. It can be clearly found that the visible-light photocatalytic activity of the nanocomposites significantly increases with the increment of the CdS content, revealing that the higher CdS content in the nanocomposites favors their visible-light photocatalytic activity.

Initial RhB concentration

Figure 12 shows the relationships between $\ln(c_0/c)$ and irradiation time at different RhB concentrations, and the inset of Fig. 12 displays the effect of initial RhB concentrations on the RhB photodegradation rates. As can be

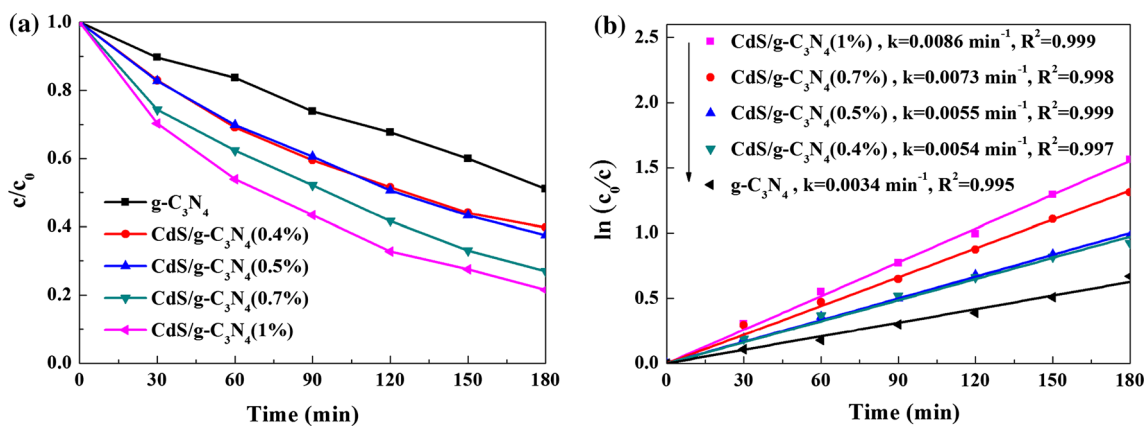


Fig. 9 Temporal course of the decrement in the RhB concentration with irradiation time (a) and relationships between $\ln(c_0/c)$ and irradiation time (b). Experimental conditions: RhB concentration (4 mg L^{-1}), catalyst concentration (1 g L^{-1})

Fig. 10 Temporal course of the decrement in the phenol concentration with irradiation time (a) and relationships between $\ln(c_0/c)$ and irradiation time (b). Experimental conditions: Phenol concentration (20 mg L^{-1}), catalyst concentration (1 g L^{-1})

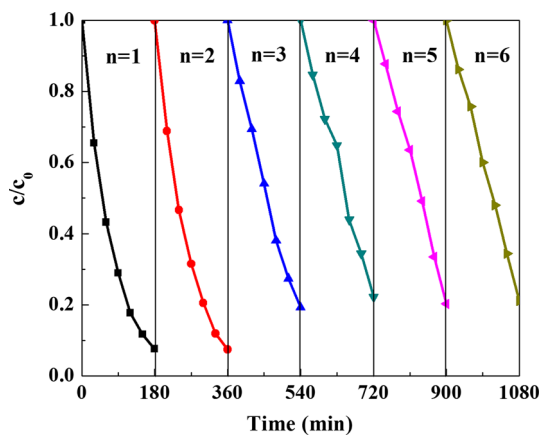
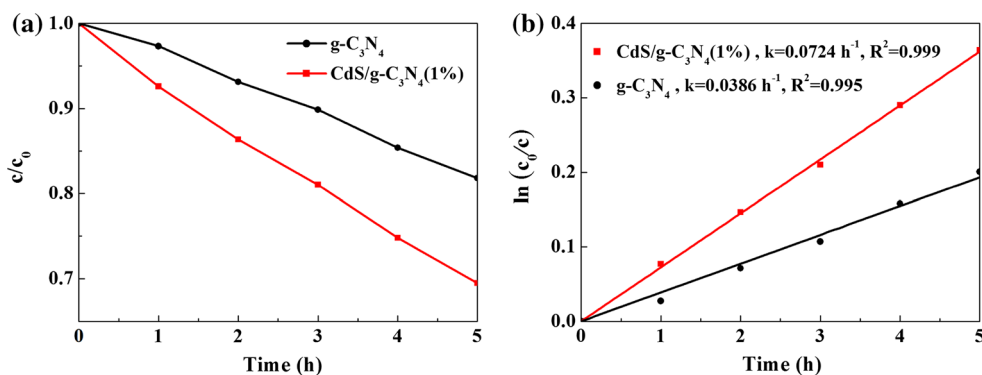


Fig. 11 Effect of cycling runs on RhB degradation in the presence of $CdS/g-C_3N_4$ (1%) under visible-light irradiation

clearly seen, the initial RhB photodegradation rate increases at first and then decreases, and reaches the maximum value when the initial RhB concentration is 4 mg L^{-1} . Generally, the RhB photodegradation rate is possibly affected by both the adsorption amount of RhB on the photocatalyst surface and photo-adsorbed ability of the

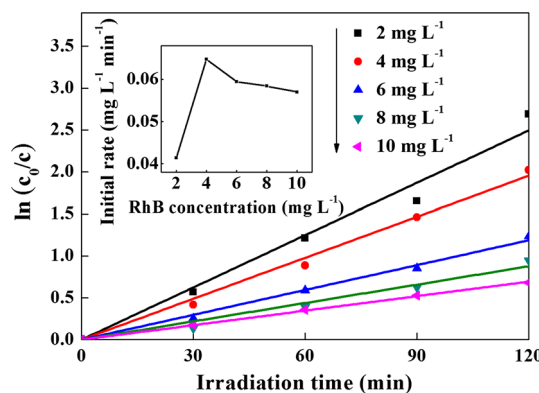


Fig. 12 Influence of the initial RhB concentrations on the RhB photodegradation rates (The inset shows the initial photodegradation rate as a function of initial RhB concentration). Experimental conditions: Catalyst concentration (1 g L^{-1})

photocatalysts. The increasing adsorption of RhB and photo-adsorbed capacity are advantageous to the photocatalytic degradation of RhB. As the initial RhB concentration increases, the adsorbed amount of RhB on the photocatalyst's surface increases, while the photo-adsorbed ability of the photocatalysts decreases because of the

decrement in the transmittance of RhB solutions. When the initial RhB concentration increases from 2 to 4 mg L⁻¹, the adsorption amount of RhB on the photocatalyst surface changes more significantly (from 526 to 1839 μg g⁻¹) than the transmittance of RhB solutions (from 38 to 15 %) (Figs. S4 and S5), indicating that the adsorption amount of RhB on the photocatalyst surface is the main affecting factor for the RhB photodegradation, thus the initial RhB photodegradation rate increases. When the initial concentration of RhB is over 4 mg L⁻¹, the adsorption of RhB on photocatalyst surface changes less (from 1839 to 2374 μg g⁻¹) than the transmittance of RhB solutions (from 15 to 1 %) (Figs. S4 and S5), and the transmittance of the RhB becomes the main affecting factor, so the photocatalytic degradation rate of MO begins to decrease.

pH value

Figure 13 presents the effect of pH value of the investigated systems on the RhB photodegradation rate under visible light, revealing that the visible-light photocatalytic activity of the CdS/g-C₃N₄ nanocomposites decreases with the pH value increasing. The result can be explained as follows. The strong interaction exists between g-C₃N₄ and RhB molecules due to -N= in g-C₃N₄ and -COOH in RhB (The RhB molecular structure can be seen in Fig. S6), leading to high adsorption of RhB on the g-C₃N₄ surface, which is advantageous to the visible-light photocatalytic activity of photocatalysts. As the pH value of the investigated systems increases, the groups of -COOH in RhB gradually change into -COO⁻, leading to the decreasing interaction between g-C₃N₄ and RhB. This decreasing interaction can reduce the adsorption of RhB on the photocatalyst surface (Fig. S7), which is disadvantageous to the visible-light photocatalytic activity of the CdS/g-C₃N₄

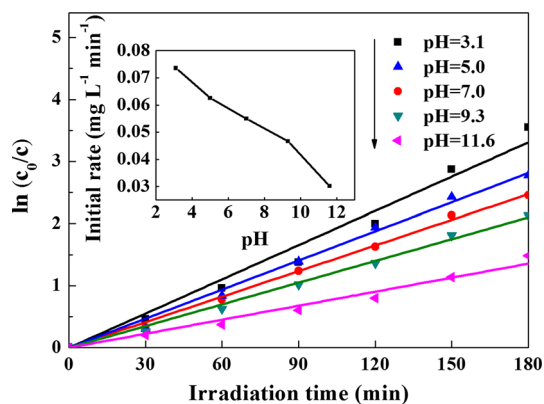


Fig. 13 Influence of pH value on the RhB photodegradation rate (The inset shows the initial photodegradation rate as a function of pH value). Experimental conditions: catalyst concentration (1 g L⁻¹), initial RhB concentration (4 mg L⁻¹)

photocatalysts. Therefore, the RhB photodegradation rate under visible light can be obviously decreased by increasing the pH value of the instigated systems.

Concentration of CdS/g-C₃N₄ nanocomposites

The effect of concentration of CdS/g-C₃N₄ nanocomposites on their visible-light photocatalytic activity is shown in Fig. 14. As the concentration of CdS/g-C₃N₄ nanocomposites increases, their visible-light photocatalytic degradation rates increase obviously due to the larger amount of active sites on the investigated photocatalysts.

Photocatalytic mechanism of CdS/g-C₃N₄ nanocomposites

The energy gaps of CdS and g-C₃N₄ are well known to be ca. 2.5 and 2.7 eV, respectively, so both CdS and g-C₃N₄ can easily absorb visible light and be excited to produce photogenerated holes and electrons [45, 46]. The photogenerated electrons in conduction band (CB) of g-C₃N₄ and CdS can react with O₂ to form •O₂⁻ due to the negative CB potentials of g-C₃N₄ (-1.13 V) and CdS (-0.48 V), and the radicals of •O₂⁻ can further react with H⁺ to form •OH [47, 48]. The photogenerated holes in valence band (VB) of both CdS and g-C₃N₄ can directly degrade RhB molecules [48]. The holes, •O₂⁻, and •OH can be responsible for the degradation of organic compounds.

The photogenerated electrons in CB of g-C₃N₄ (-1.13 V) can be easily injected into CB of CdS (-0.43), and the photogenerated holes in VB of CdS (2.02 V) can efficiently transfer to VB of g-C₃N₄ (1.57 eV). This means more efficient separation between the photogenerated holes and electrons in CdS/g-C₃N₄ nanocomposite photocatalysts, which is advantageous to their visible-light photocatalytic activity. Therefore, the visible-light photocatalytic

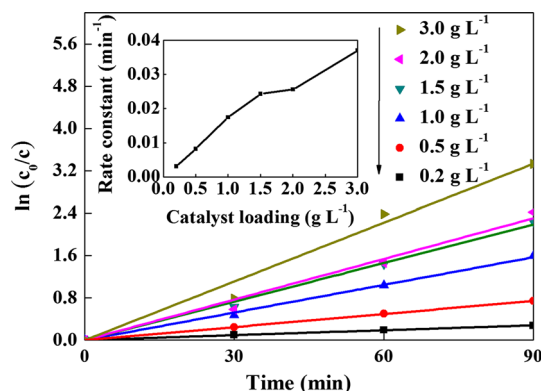


Fig. 14 Effect of the concentration of CdS/g-C₃N₄ nanocomposites on the RhB photodegradation rate. Experimental conditions: Initial RhB concentration (4 mg L⁻¹)

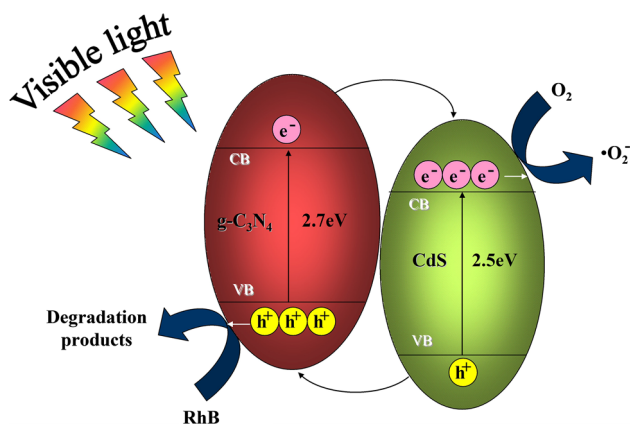
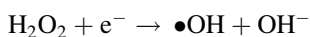
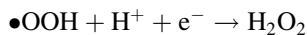
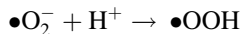
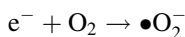
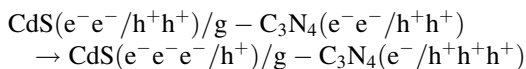
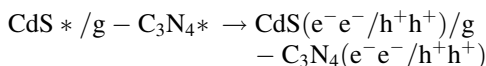
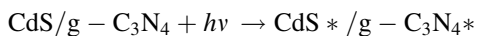


Fig. 15 The proposed visible-light photocatalytic mechanism of CdS/g-C₃N₄ nanocomposites

activity of the CdS/g-C₃N₄ nanocomposites is much higher than that of pure g-C₃N₄. The proposed photocatalytic mechanism of the CdS/g-C₃N₄ nanocomposites is schematically shown in Fig. 15, and the major possible reactions for the RhB photodegradation are displayed as follows.



Conclusions

An efficient visible-light photocatalyst was successfully synthesized by surface-hybridization of g-C₃N₄ using a small amount of CdS nanoparticles. The surface-hybridization of CdS nanoparticles with the content of <1 % is able to obviously improve the absorbance of g-C₃N₄ particles in the visible light range and separation efficiency of photogenerated electron/hole pairs in the nanocomposites, while hardly affects their crystallinity and nanocrystal size. The visible-light photocatalytic activity of CdS/g-

C₃N₄ nanocomposites is much higher than that of pure g-C₃N₄, and increases with the increment in both CdS content on the nanocomposites and photocatalyst concentration, while increases at first and then decreases with the increment in both initial RhB concentration and pH value of the investigated system. The cycled experiments reveal that the visible-light photocatalytic stability of the investigated nanocomposites is good. Therefore, it is a facile method to prepare an efficient visible-light photocatalyst by the surface-hybridization of g-C₃N₄ using a small amount of CdS nanoparticles.

Acknowledgements This work was supported by the National Natural Science Foundation of China (21271061) and Natural Science Foundation of Hebei Province (B2014208103).

References

1. Fujishima A, Honda K (1972) Electrochemical photolysis of water at a semiconductor electrode. *Nature* 238:37–38
2. Hoffmann MR, Martin ST, Choi W, Bahnemann DW (1995) Environmental applications of semiconductor photocatalysis. *Chem Rev* 95:69–96
3. Chen C, Ma W, Zhao J (2010) Semiconductor-mediated photodegradation of pollutants under visible-light irradiation. *Chem Soc Rev* 39:4206–4219
4. Pawar RC, Lee CS (2014) Single-step sensitization of reduced graphene oxide sheets and CdS nanoparticles on ZnO nanorods as visible-light photocatalysts. *Appl Catal B* 144:57–65
5. Pawar RC, Lee CS (2013) Sensitization of CdS nanoparticles onto reduced graphene oxide (RGO) fabricated by chemical bath deposition method for effective removal of Cr(VI). *Mater Chem Phys* 141:686–693
6. Fujishima A, Rao TN, Tryk DA (2000) Titanium dioxide photocatalysis. *J Photochem Photobio C* 1:1–21
7. Nakata K, Fujishima A (2012) TiO₂ photocatalysis: design and applications. *J Photochem Photobio C* 13:169–189
8. Lee SY, Park SJ (2013) TiO₂ photocatalyst for water treatment applications. *J Ind Eng Chem* 19:1761–1769
9. Dholam R, Patel N, Adami M, Miotello A (2009) Hydrogen production by photocatalytic water-splitting using Cr- or Fe-doped TiO₂ composite thin films photocatalyst. *Int J Hydrog Energy* 34:5337–5346
10. Charanpahari A, Umare SS, Sasikala R (2013) Effect of Ce, N and S multi-doping on the photocatalytic activity of TiO₂. *Appl Surf Sci* 282:408–414
11. Li XY, Wang DS, Cheng GX, Luo QZ, An J, Wang YH (2008) Preparation of polyaniline-modified TiO₂ nanoparticles and their photocatalytic activity under visible light illumination. *Appl Catal B* 81:267–273
12. Luo QZ, Bao LL, Wang DS, Li XY, An J (2012) Preparation and strongly enhanced visible light photocatalytic activity of TiO₂ nanoparticles modified by conjugated derivatives of polyisoprene. *J Phys Chem C* 116:25806–25815
13. Mehraj O, Mir NA, Pirzada BM, Sabir S, Muneer M (2014) In-situ anion exchange synthesis of AgBr/Ag₂CO₃ hybrids with enhanced visible light photocatalytic activity and improved stability. *J Mol Catal A* 395:16–24
14. Luo L, Li YZ, Hou JT, Yang Y (2014) Visible photocatalysis and photostability of Ag₃PO₄ photocatalyst. *Appl Surf Sci* 319:332–338

15. Duan YD, Luo QZ, Wang DS, Li XY, An J, Liu Q (2014) An efficient visible light photocatalyst poly(3-hexylthiophene)/CdS nanocomposite with enhanced antiphotocorrosion property. *Superlattices Microstruct* 67:61–71
16. Pu YF, Li YZ, Huang YL, Kim SI, Cai PQ, Seo HJ (2015) Visible light-induced degradation of methylene blue by photocatalyst of bismuth layered $\text{Bi}_7\text{VO}_{13}$ nanoparticles. *Mater Lett* 141:73–75
17. Cui WQ, An WJ, Liu L, Hu JS, Liang YH (2014) Synthesis of CdS/BiOBr composite and its enhanced photocatalytic degradation for Rhodamine B. *Appl Surf Sci* 319:298–305
18. Yang YX, Guo YN, Liu FY, Yuan X, Guo YH, Zhang SQ, Guo W, Huo MX (2013) Preparation and enhanced visible-light photocatalytic activity of silver deposited graphitic carbon nitride plasmonic photocatalyst. *Appl Catal B* 142–143:828–837
19. Michael RW (1990) Chemical preparation and shock wave compression of carbon nitride precursors. *J Am Ceram Soc* 73:1973–1978
20. Dong G, Zhang Y, Pan Q, Qiu J (2014) A fantastic graphitic carbon nitride (g- C_3N_4) material: electronic structure, photocatalytic and photoelectronic properties. *J Photochem Photobiol C* 20:33–50
21. Chen J, Shen SH, Guo PH, Wang M, Wu P, Wang XX, Guo LJ (2014) In-situ reduction synthesis of nano-sized Cu_2O particles modifying g- C_3N_4 for enhanced photocatalytic hydrogen production. *Appl Catal B* 152–153:335–341
22. Zhang SQ, Yang YX, Guo YN, Guo W, Wang M, Guo YH, Huo MX (2013) Preparation and enhanced visible-light photocatalytic activity of graphitic carbon nitride/bismuth niobate heterojunctions. *J Hazard Mater* 261:235–245
23. Zhu GZ, Lv K, Sun Q, Kawazoe Y, Jena P (2014) Lithium-doped triazine-based graphitic C_3N_4 sheet for hydrogen storage at ambient temperature. *Comput Mater Sci* 81:275–279
24. Cao SW, Yuan YP, Barber J, Loo SCJ, Xue C (2014) Noble-metal-free g- $\text{C}_3\text{N}_4/\text{Ni}(\text{dmgH})_2$ composite for efficient photocatalytic hydrogen evolution under visible light irradiation. *Appl Surf Sci* 319:344–349
25. Zhong YJ, Wang ZQ, Feng JY, Yan SC, Zhang HT, Li ZS, Zou ZG (2014) Improvement in photocatalytic H_2 evolution over g- C_3N_4 prepared from protonated melamine. *Appl Surf Sci* 295:253–259
26. Katsumata K, Motoyoshi R, Matsushita N, Okada K (2013) Preparation of graphitic carbon nitride (g- C_3N_4)/ WO_3 composites and enhanced visible-light-driven photodegradation of acetaldehyde gas. *J Hazard Mater* 260:475–482
27. Pawar RC, Khare V, Lee CS (2014) Hybrid photocatalysts using graphitic carbon nitride/cadmium sulfide/reduced graphene oxide (g- $\text{C}_3\text{N}_4/\text{CdS}/\text{RGO}$) for superior photodegradation of organic pollutants under UV and visible light. *Dalton Trans* 43:12514–12527
28. Akhundi A, Habibi-Yangjeh A (2015) Novel magnetically separable g- $\text{C}_3\text{N}_4/\text{AgBr}/\text{Fe}_3\text{O}_4$ nanocomposites as visible-light-driven photocatalysts with highly enhanced activities. *Ceram Int* 41:5634–5643
29. Akhundi A, Habibi-Yangjeh A (2015) Novel magnetic g- $\text{C}_3\text{N}_4/\text{Fe}_3\text{O}_4/\text{AgCl}$ nanocomposites: facile and large-scale preparation and highly efficient photocatalytic activities under visible-light irradiation. *Mater Sci Semicond Process* 39:162–171
30. Zhao Z, Sun Y, Dong F (2015) Graphitic carbon nitride based nanocomposites: a review. *Nanoscale* 7:15–37
31. Zhang SW, Zhao LP, Zeng MY, Li JX, Xu JZ, Wang XK (2014) Hierarchical nanocomposites of polyaniline nanorods arrays on graphitic carbon nitride sheets with synergistic effect for photocatalysis. *Catal Today* 224:114–121
32. Vu TTD, Mighri F, Ajji A, Do TO (2014) Synthesis of titanium dioxide/cadmium sulfide nanosphere particles for photocatalyst applications. *Ind Eng Chem Res* 53:3888–3897
33. Ge L, Zuo F, Liu JK, Ma Q, Wang C, Sun DZ, Bartels L, Feng P (2012) Synthesis and efficient visible light photocatalytic hydrogen evolution of polymeric g- C_3N_4 coupled with CdS quantum dots. *J Phys Chem C* 116:13708–13714
34. Zhang JY, Wang YH, Jin J, Zhang J, Lin Z, Huang F, Yu JG (2013) Efficient visible-light photocatalytic hydrogen evolution and enhanced photostability of core/shell CdS/g- C_3N_4 nanowires. *ACS Appl Mater Interfaces* 5:10317–10324
35. Cao SW, Yuan YP, Fang J, Shahjamali MM, Boey FYC, Barber J, Loo SCJ, Xue C (2013) In-situ growth of CdS quantum dots on g- C_3N_4 nanosheets for highly efficient photocatalytic hydrogen generation under visible light irradiation. *Int J Hydrog Energy* 38:1258–1266
36. Fu J, Chang BB, Tian YL, Xi FN, Dong XP (2013) Novel C_3N_4 -CdS composite photocatalysts with organic-inorganic heterojunctions: in situ synthesis, exceptional activity, high stability and photocatalytic mechanism. *J Mater Chem A* 1:3083–3090
37. Jiang F, Yan TT, Chen H, Sun AW, Xu CM, Wang X (2014) Ag- C_3N_4 -CdS composite catalyst with high visible-light-driven catalytic activity and photostability for methylene blue degradation. *Appl Surf Sci* 295:164–172
38. Dai X, Xie ML, Meng SG, Fu XL, Chen SF (2014) Coupled systems for selective oxidation of aromatic alcohols to aldehydes and reduction of nitrobenzene into aniline using CdS/g- C_3N_4 photocatalyst under visible light irradiation. *Appl Catal B* 158–159:382–390
39. Wang XC, Maeda K, Thomas A, Takanabe K, Xin G, Carlsson JM, Domen K, Antonietti M (2009) A metal-free polymeric photocatalyst for hydrogen production from water under visible light. *Nat Mater* 8:76–82
40. Wang Y, Wang XC, Antonietti M (2012) Polymeric graphitic carbon nitride as a heterogeneous organocatalyst: from photochemistry to multipurpose catalysis to sustainable chemistry. *Angew Chem Int Ed* 51:68–89
41. Niu P, Liu G, Cheng HM (2012) Nitrogen vacancy-promoted photocatalytic activity of graphitic carbon nitride. *J Phys Chem C* 116:11013–11018
42. Liu Y, Yu YX, Zhang WD (2014) Photoelectrochemical study on charge transfer properties of nanostructured Fe_2O_3 modified by g- C_3N_4 . *Int J Hydrog Energy* 39:9105–9113
43. Zhao JL, Ji ZY, Shen XP, Zhou H, Ma LB (2015) Facile synthesis of WO_3 nanorods/g- C_3N_4 composites with enhanced photocatalytic activity. *Ceram Int* 41:5600–5606
44. Wang DS, Sun HT, Luo QZ, Yang XL, Yin R (2014) An efficient visible-light photocatalyst prepared from g- C_3N_4 and polyvinyl chloride. *Appl Catal B* 156–157:323–330
45. Hagfeldt A, Gratzel M (1995) Light-induced redox reactions in nanocrystalline systems. *Chem Rev* 95:49–68
46. Zhang JS, Chen XF, Takanabe K, Maeda K, Domen K, Epping JD, Fu XZ, Antonietti M, Wang XC (2010) Synthesis of a carbon nitride structure for visible-light catalysis by copolymerization. *Angew Chem Int Ed* 49:441–444
47. Mousavi M, Habibi-Yangjeh A (2015) Ternary g- $\text{C}_3\text{N}_4/\text{Fe}_3\text{O}_4/\text{Ag}_3\text{VO}_4$ nanocomposites: novel magnetically separable visible-light-driven photocatalysts for efficiently degradation of dye pollutants. *Mater Chem Phys*. doi:10.1016/j.matchemphys.2015.07.061
48. Li G, Wong KH, Zhang X, Hu C, Yu JC, Chan RCY, Wong PK (2009) Degradation of Acid Orange 7 using magnetic AgBr under visible light: the roles of oxidizing species. *Chemosphere* 76:1185–1191